

# MRI-based brain tumor detection and types of classification using CEHJB-RI and JMST

*Uma Shankar Kommanaboina*<sup>1\*</sup>, *Sandeep Tummalsugur*<sup>2</sup>, and *Shirisha Kommanaboina*<sup>3</sup>,  
*G.vijendar reddy*<sup>4</sup>, *Kseniia Iurevna Usanova*<sup>5</sup>

<sup>1</sup>Computer Science and Engineering, KG Reddy College of Engineering & Technology, Hyderabad, India.

<sup>2</sup>Information Technology, Stanley College of Engineering and Technology for Women, Hyderabad, India.

<sup>3</sup>Computer Science and Engineering, AVN Institute of Engineering & Technology, Hyderabad, India

<sup>4</sup>Department of IT, GRIET, Hyderabad, Telangana, India

<sup>5</sup>Lovely Professional University, Phagwara, Punjab, India.

**Abstract.** The Brain Tumor (BT), which forms in the brain cells and spreads to the whole brain, may lead to death. Hence, early diagnosis of BT is significant. Still, the detection of BT between the skull and brain region is not concentrated, which results in misclassification outcomes. Thus, this article proposes Magnetic Resonance Imaging (MRI)-based BT detection and types' classification utilizing Carlitz Exponential Hamilton Jacobi Bellman-based Reinforcement Learning (CEHJB-RL) and JenSorensen similarity-based Minimum Spanning Tree (JMST). Primarily, raw MRI images are taken and then pre-processed. Then, with skull and without skull regions are extracted from the pre-processed image and are subjected to the graph construction. Conversely, the edges are detected from the pre-processed image that can be patch-extracted and subjected to graph construction. By utilizing JMST and Morphological Operations (MO), the graphs are constructed. Thereafter, the features are extracted and fed to the classifier. Then, the type of BT is classified by the classifier using CEHJB-RL. Concerning the performance metrics, the outcomes illustrated that the proposed technique attained a higher accuracy (99.27%), which is better than other existing techniques.

## 1 Introduction

The brain, which comprises billions of cells, is an important organ of the human body [1]. BT is caused by the cells' abnormal growth in the human brain [2]. BT is fundamentally identified utilizing computed tomography, positron emission tomography, and MRI [3]. Among these, MRI has harmless magnetic fields and radio waves. Hence, it is very efficient for BT detection [4]. Meningioma, pituitary, and glioma are the various types of BT. Among these, gliomas are the increasing BT, which affects the human mortality rate [5, 6]. Thus, to identify the type of tumor and undergo further treatment, early BT detection is essential [7].

To classify the medical images for detecting the type of BT, Machine Learning (ML) mechanisms, namely Support Vector Machines (SVM) are utilized in existing studies. However, SVM takes more time for training [8]. Therefore, to diagnose the BT from MR images, Deep Learning (DL) approaches like Long Short Term Memory, Convolutional Neural Network (CNN), and Deep CNN (DCNN) are suggested. However, they are affected by overfitting problems [9, 10]. Hence, to detect the BT between the skull and brain regions, improvement is still required. Therefore, this work proposes MRI-based BT detection and types' classification using CEHJB-RL.

## 1.1 Problem Statement

Prevailing techniques have some limitations, such as:

- ✓ The identification of BTs between the skull and brain region was not concentrated.
- ✓ There was an issue of properly segregating the brain and skull regions in existing works.
- ✓ Most of the existing works did not consider the missing finite information losses during Patch Extraction (PE).
- ✓ In prevailing works, stroke lesion segmentation was a complex task.

This paper considered some research objectives, such as:

- ✓ To identify the BTs between the skull and brain regions, with skull stripping and without skull stripping are performed.
- ✓ For the proper segregation of brain and skull regions, JMST graph construction is utilized.
- ✓ PE and MO are introduced to consider the missing finite information losses.
- ✓ JMST is used to superiorly segment the stroke lesions.

The remaining paper is structured as: the related works are summarized in section 2; section 3 illustrates the proposed system; the outcomes are exemplified in section 4; the paper is wrapped up in section 5.

## 2 Literature Survey

**Rehman et al. [11]** employed 3D CNN as well as feature selection architecture to classify the BT. Here, to identify the BT, 3D CNN with correlation-centric feature selection was utilized. In the classification of BT, this model performed well. Nevertheless, more datasets were utilized by the 3D CNN. Hence, the memory requirement was increased, which made the model more complex.

**Irmak [12]** elucidated the MRI-based multi-classification of BT using DCNN. To classify the BT, all the hybrid parameters of CNN were employed. This system superiorly classified the BT into glioma, meningioma, and pituitary. Also, the Training Time (TT) was increased when too many images were processed, thus slowing down the performance of this model.

**Mostafiz et al. [13]** described the MRI-based BT identification using CNN-based neural features. To obtain the most relevant features, this model utilized the principle component analysis. Therefore, this fusion method gave a better performance. However, this model directly passed the raw input to the classifier. Hence, the raw input data had more noise, which might produce errors during classification.

**Jia & Chen, [14]** utilized DL techniques for identifying and classifying the BT in MRI images. To segment the BT, SVM was employed. In detecting normal and abnormal tissue from brain MRI, this model achieved better outcomes. Yet, the interpretation of the SVM model was difficult. Also, it took a long time for large datasets, thus affecting the system's performance.

**Kalaiselvi et al. [15]** propounded the BT detection model using CNN from MRI. Here, six CCN models were utilized, which were tested and trained utilizing the WBA dataset and BraTS2013 dataset, respectively. The tumor slices were efficiently classified by this model. However, to execute all of the six CNN models, this model took a long time, which led to complexities in the model.

### 3 Proposed BT Detection and Types' Classification System

The proposed model utilizes CEHJB-RL to detect and classify the types of BT grounded on MRI images shown in figure 1.

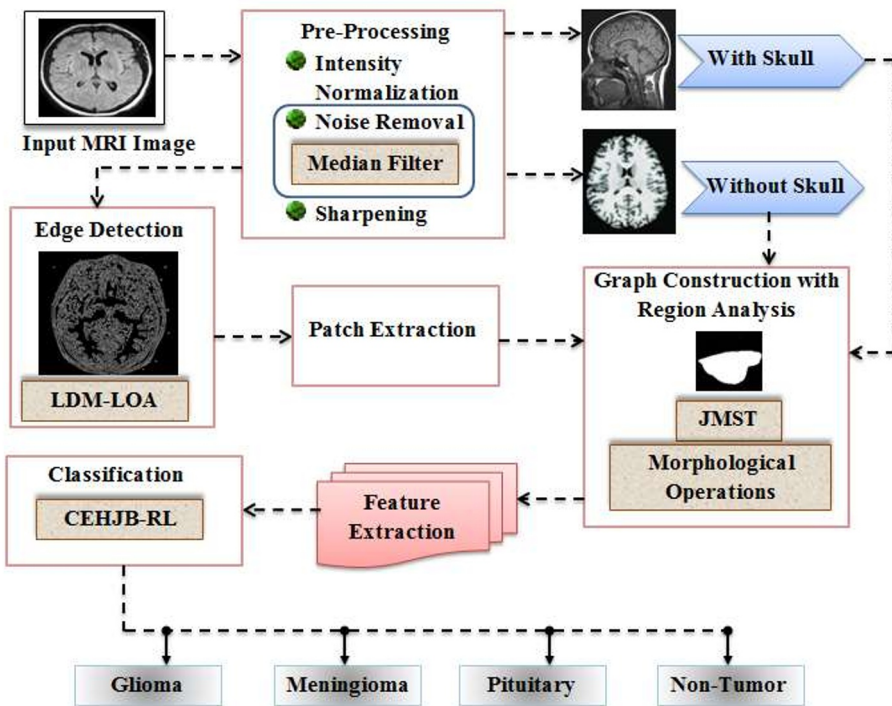


Fig. 1. The architecture diagram of the proposed model

#### 3.1 Input MRI Image

Firstly, the raw MRI image is taken as input, which is represented in equation (1),

$$A_v = \{A_1, A_2, A_3, \dots, A_\ell\} \quad \text{where } v = 1, 2, 3, \dots, \ell \quad (1)$$

Where,  $A_v$  is the total  $\ell$  number of input images.

### 3.2 Pre-Processing

Next, to enrich the image quality, the input MRI images are pre-processed.

#### 3.2.1 Intensity Normalization

Primarily, to ensure compatibility across the images, intensity normalization is performed on  $A_v$ . The  $A_v$  are intensity normalized concerning maximum  $\max(A_v)$  and minimum  $\min(A_v)$  values at a range of 0 or 1. It can be articulated as mentioned in equation (2),

$$\Omega(A_v) = \frac{A_v - \min(A_v)}{\max(A_v) - \min(A_v)} \quad (2)$$

Where,  $\Omega$  exemplifies the intensity normalized image.

#### 3.2.2 Noise Removal

Next, from the  $\Omega$ , the unwanted noises are removed using a Median Filter (MF). MF is very efficient in smoothing the spiky noises, which can be derived using the following equation (3),

$$\mathfrak{R}(\Omega) = \frac{\left(\frac{\Omega}{2}\right) + \left(\frac{\Omega}{2} + 1\right)}{2} \quad (3)$$

Here,  $\mathfrak{R}$  specifies the filtered image.

#### 3.2.3 Sharpening

Afterward, to enrich the quality of the image and its edges, the  $\mathfrak{R}$  is sharpened. It can be equated as shown in equation (4),

$$\mathfrak{N}_\forall = [\mathfrak{N}_1, \mathfrak{N}_2, \mathfrak{N}_3, \dots, \mathfrak{N}_\varphi] \quad \text{Here } \forall = 1, 2, 3, \dots, \varphi \quad (4)$$

Where,  $\mathfrak{N}_\forall$  symbolizes the sharpened image, which exemplifies the final pre-processed image.

### 3.3 Skull Stripping

To effectively identify the BT between the skull and brain regions, with skull and without skull regions are extracted from  $\mathfrak{N}_\forall$ . With skull-stripped  $D_m^\circ$  and without skull-stripped  $S_\varepsilon^\circ$  images can be described as mentioned in equations (5) and (6),

$$D_m^\circ(\mathfrak{N}_\forall) = (D_1^\circ, D_2^\circ, D_3^\circ, \dots, D_f^\circ) \quad (5)$$

$$S_\varepsilon^\circ(\mathfrak{N}_\forall) = (S_1^\circ, S_2^\circ, S_3^\circ, \dots, S_g^\circ) \quad (6)$$

Where, the total  $f$  number of with skull-stripped images is signified as  $D_f^\circ$ , and the total  $g$  number of without skull-stripped images is notated as  $S_g^\circ$ .

### 3.4 Edge Detection

In the meantime, for enhancing the classification accuracy, the edges are detected from  $\mathfrak{S}_\nabla$ . Here, to efficiently detect the edges, the Linear Density Matrix-Lyrebird Optimization Algorithm (LDM-LOA) algorithm is utilized. Lyrebird Optimization Algorithm (LOA) finds the optimal global solution by using its escaping strategy. However, during random positioning, the lyrebird loses its efficiency in the escaping strategy. To overcome these issues, the Linear Density Matrix (LDM) is utilized for position identification. Firstly, the population of lyrebirds is initialized. The initialized population  $\mathfrak{S}$  is the detected edges, which can be described as mentioned in equations (7) and (8),

$$\mathfrak{S} = \begin{bmatrix} \mathfrak{S}_1 \\ \mathfrak{S}_p \\ \mathfrak{S}_B \end{bmatrix}_{B \times C} = \begin{bmatrix} \tilde{\lambda}_{1,1} & \tilde{\lambda}_{1,q} & \tilde{\lambda}_{1,C} \\ \tilde{\lambda}_{p,1} & \tilde{\lambda}_{p,q} & d'_{p,C} \\ \tilde{\lambda}_{B,1} & d'_{B,q} & d'_{B,C} \end{bmatrix}_{B \times C} \quad (7)$$

$$\tilde{\lambda}_{p,q} = lb_q + r_{p,q} \bullet (ub_q - lb_q) \quad (8)$$

Wherein,  $\mathfrak{S}_p$  specifies the  $p^{th}$  lyrebird,  $\tilde{\lambda}_{p,q}$  epitomizes the  $q^{th}$  dimension of the problem, where  $p = 1, 2, 3, \dots, B$  and  $q = 1, 2, 3, \dots, C$ . Here, the random numbers are represented as  $r_{p,q}$ , and  $lb_q$  and  $ub_q$  signify the lower and upper bound values. The fitness value  $F$  regarding maximum standard deviation is equated as mentioned in equation (9),

$$F = \max \left( \sqrt{\frac{\sum (\mathfrak{S} - \gamma)^2}{\mathfrak{S}_p}} \right) * \begin{bmatrix} F_1 \\ F_p \\ F_B \end{bmatrix}_{B \times 1} = \begin{bmatrix} F(\mathfrak{S}_1) \\ F(\mathfrak{S}_p) \\ F(\mathfrak{S}_B) \end{bmatrix}_{B \times 1} \quad (9)$$

$$\mathfrak{S}_{best} = best(F) \quad (10)$$

Here,  $\mathfrak{S}_{best}$  as shown in equation (10) is the best candidate solution. In the exploration phase, lyrebirds escape and move to safe areas. To increase the exploration power, the LDM is replaced. Thereafter, the exploration  $K_p$  of each lyrebird is articulated as expressed in equation (11),

$$K_p = \left( \sum \tilde{\lambda}_{p,q} * \frac{|\mathfrak{S}_p - \mathfrak{S}_B|^2}{|\mathfrak{S}_B - \mathfrak{S}_p|} \right) \cup \{ \mathfrak{S}_{best} \} \quad (11)$$

Afterward, the updated new position  $\tilde{\lambda}_{p,q}^n$  of the corresponding lyrebird is equated as shown in equation (12),

$$\tilde{\lambda}_{p,q}^n = \tilde{\lambda}_{p,q} + r_{p,q} \bullet (H_{p,q} - J_{p,q} \bullet \tilde{\lambda}_{p,q}) \quad (12)$$

Here, the  $q^{th}$  dimension is specified as  $H_{p,q}$ , and the random number is symbolized as  $J_{p,q}$ . The updated  $p^{th}$  position is given as represented in equation (13),

$$\mathfrak{S}_p = \begin{cases} \text{if } F_p^n < F_p & \tilde{\lambda}_{p,q}^n \\ \text{else} & \mathfrak{S}_p \end{cases} \quad (13)$$

Wherein,  $F_p^n$  is the fitness. In the exploitation phase, the suitable position  $\tilde{\lambda}_{p,q}^s$  is updated grounded on the modelling strategy of the lyrebird to hide, which is defined as formulated in (14) and (15) equations,

$$\tilde{\lambda}_{p,q}^s = \tilde{\lambda}_{p,q} + \frac{lb_q + r \bullet (ub_q - lb_q)}{it} \quad (14)$$

$$\mathfrak{S}_p = \begin{cases} \text{if } F_p^s < F_p & \tilde{\lambda}_{p,q}^s \\ \text{else} & \mathfrak{S}_p \end{cases} \quad (15)$$

Here, the present and maximum iterations are symbolized as  $it$  and  $it_{max}$ , respectively, and  $F_p^s$  is the fitness of the  $\tilde{\lambda}_{p,q}^s$ . This update process is continued until the last iteration. Lastly, the edge-detected image  $\Theta_d$  can be explicated as mentioned in equation (16),

$$\Theta_d = \{\Theta_1, \Theta_2, \Theta_3, \dots, \Theta_{ab}\} \quad (16)$$

Where,  $ab$  specifies the total number of  $\Theta_d$ .

#### Pseudocode for CA-OOA

---

**Input:** Pre-processed image  $\mathfrak{S}_v$

**Output:** Edge-detected image  $\Theta_d$

---

**Begin**

**Initialize** population  $\mathfrak{S}$

**While**  $it \leq it_{max}$

**For each**  $\mathfrak{S}$

**Find** dimension  $\tilde{\lambda}_{p,q}$

**Calculate**  $\mathfrak{S}_{best} = best(F)$

**Update** new position

**If**  $F_p^n < F_p$

$\tilde{\lambda}_{p,q}^n$

```

        Else
             $\mathfrak{S}_p$ 
        End If
        Update new suitable position
        If  $F_p^s < F_p$ 
             $\lambda_{p,q}^s$ 
        Else
             $\mathfrak{S}_p$ 
        End If
    End For
End While
Obtain  $\Theta_d$ 
    
```

**End**

After that,  $\Theta_d$  are subjected to PE, which is explained further:

### 3.5 Patch Extraction

Then, to improve the classification, PE is performed to extract a set of sub-images from  $\Theta_d$ . The patch-extracted image  $T_k^*$  is described as shown in the equation (17),

$$T_k^*(\Theta_d) = \{T_1^*, T_2^*, T_3^*, \dots, T_x^*\} \quad \text{Here } k = 1, 2, 3, \dots, x \quad (17)$$

Where,  $T_2^*$  signifies the second  $T_k^*$ .

### 3.6 Graph Construction with Region Analysis

Thereafter, to identify the tumor regions, the graph is constructed for the combination of  $D_m^\circ$  and  $S_\varepsilon^\circ$ , and for  $T_k^*$  by utilizing JMST. Minimum Spanning Tree (MST) is a fast as well as effective mechanism to obtain a set of segmented images that uses Euclidean similarity. However, it does not always discover more accurate clusters. Hence, to overcome this problem, Jensorensen Similarity (JS) is utilized to effectively find more accurate clusters. Afterward, the JS  $\Psi$  between  $D_m^\circ$  and  $S_\varepsilon^\circ$  is given as mentioned in the equation (18),

$$\Psi(D_m^\circ, S_\varepsilon^\circ) = \sum \frac{2|D_m^\circ \cap S_\varepsilon^\circ|}{|D_m^\circ| + |S_\varepsilon^\circ|} \quad (18)$$

After that, the weighted graph's vertices  $V_\varepsilon$  and edges  $E_\delta$  are described as mentioned in the equations (19) and (20),

$$V_\varepsilon = (V_1, V_2, V_3, \dots, V_l) \quad \text{Here } \varepsilon = 1, 2, 3, \dots, l \quad (19)$$

$$E_\delta = (E_1, E_2, E_3, \dots, E_z) \quad \text{Here } \varepsilon = 1, 2, 3, \dots, z \quad (20)$$

Afterward, the weights of all the edges can be computed using the equation (21),

$$W(E_{\delta}) = \sqrt{W_{\infty} + W_{\beta} + W_{\Delta}} \quad (21)$$

Where,  $W_{\infty}$ ,  $W_{\beta}$  and  $W_{\Delta}$  are the weighting coefficients. Next, the internal difference of  $D_m^{\circ}$  and  $S_{\varepsilon}^{\circ}$  is computed, which is described as mentioned in the equation (22),

$$I(D_m^{\circ}, S_{\varepsilon}^{\circ}) = \max (W(E_{\delta})) \quad (22)$$

Thereafter, the difference between the two regions  $U(D_m^{\circ}, S_{\varepsilon}^{\circ})$  is discovered, which is represented as shown in the equation (23),

$$U(D_m^{\circ}, S_{\varepsilon}^{\circ}) = \min W(E_{\delta}) * W(V_{\varepsilon}) \quad (23)$$

Then, the segmentation region found from  $U(D_m^{\circ}, S_{\varepsilon}^{\circ})$  and  $I(D_m^{\circ}, S_{\varepsilon}^{\circ})$  can be given as mentioned in (24) equation,

$$U(D_m^{\circ}, S_{\varepsilon}^{\circ}) \leq \text{Min}(I(D_m^{\circ}) + \tau(D_m^{\circ}), I(S_{\varepsilon}^{\circ}) + \tau(S_{\varepsilon}^{\circ})) \quad (24)$$

Where,  $\tau$  symbolizes the threshold function.  $D_m^{\circ}$  and  $S_{\varepsilon}^{\circ}$  are merged if the above equation is true; otherwise, they remain unchanged. Then, the MO is performed to eliminate small objects and thin lines from an image, thus protecting the image's shape and size. Lastly, the graph constructed for  $D_m^{\circ}$  and  $S_{\varepsilon}^{\circ}$  is notated as  $\zeta^{\Phi}$ , which is articulated as mentioned in the equation (25),

$$\zeta^{\Phi} = \{\zeta^1, \zeta^2, \zeta^3, \dots, \zeta^{\chi}\} \quad \text{where } \Phi = 1, 2, 3, \dots, \chi \quad (25)$$

Likewise, the graph constructed for  $T_k^*$  is implied as  $\hbar^{\perp}$ . Thereafter, by using the above process, the MO is done. It can be defined using the equation (26),

$$\hbar^{\perp} = \{\hbar^1, \hbar^2, \hbar^3, \dots, \hbar^{\alpha}\} \quad \text{where } \perp = 1, 2, 3, \dots, \alpha \quad (26)$$

Thus, the process of graph construction and morphological operation are described above.

### 3.7 Feature Extraction

Thereafter, from  $\zeta^{\Phi}$  and  $\hbar^{\perp}$ , the features, namely texture features, histogram of oriented gradient features, grey level co-occurrence matrix features, and statistical features are extracted. The extracted features  $\eta_{\pi}$  can be expressed as represented in the equation (27),

$$\eta_{\pi}(\zeta^{\Phi}, \hbar^{\perp}) = [\eta_1, \eta_2, \eta_3, \dots, \eta_t] \quad \text{where } \pi = 1, 2, 3, \dots, t \quad (27)$$

Here,  $\eta_t$  signifies the total  $t$  number of  $\eta_{\pi}$ .

### 3.8 Classification

Finally, to classify the types of BT,  $\eta_{\pi}$  are classified utilizing CEHJB-RL. Reinforcement Learning (RL) can solve very complex problems. However, RL agents are affected by computational complexities and memory issues. Hence, for improving efficiency, Carlitz

Exponential Hamilton Jacobi Bellman (CEHJB) is included to update policy  $Q$ . CEHJB-RL's structural diagram is shown in the Fig. 2.

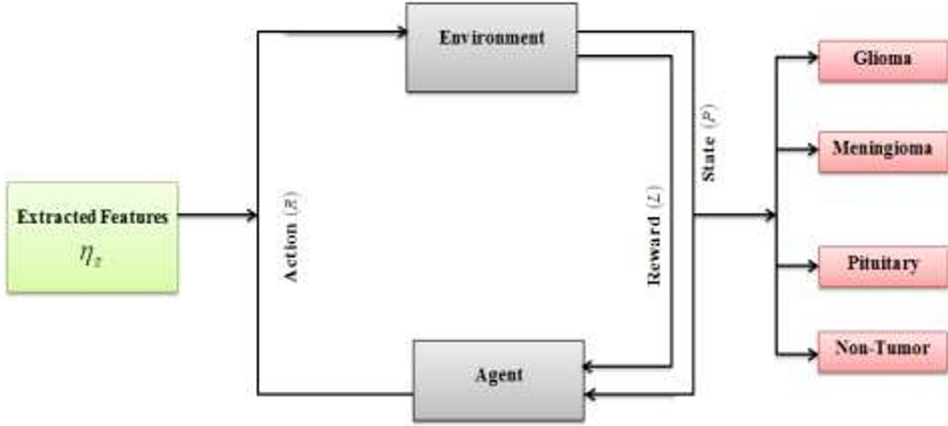


**Fig. 2.** Structural diagram of CEHJB-RL

The CEHJB-RL comprises policy, reward, state, and action. Primarily, the value function  $v_Q$  under the policy  $Q(R | P)$  is evaluated, which is articulated as shown in equation (28),

$$v_Q = \sum_R Q(R | P) \sum_{P',L} b(P', L | P, R) [L + \gamma' v_Q(P')] \quad (28)$$

Where,  $P'$  symbolizes the new state,  $L$  signifies the reward,  $R$  is the action,  $\gamma'$  exemplifies the risk factor, and  $b$  specifies the learning co-efficient. Here, to improve the efficiency of RL, the  $Q$  value is updated grounded on CEHJB, and it can be expressed as mentioned in the equation (29),

$$N = \frac{1}{k} \sum \frac{v_Q(P) \times \log(Q(R | P))}{L} \quad (29)$$

Here,  $N$  epitomizes the updation process of  $Q$  value and  $k$  is the constant. The high reward is considered as the negative class label. If the reward is a negative class label, then the agent should continue the process until it becomes a positive class label. Lastly, the state delivers the outcomes of the BT types.

### Pseudo-code for CEHJB-RL

**Input:** Extracted features  $\eta_\pi$

**Output:** Glioma, Meningioma, Pituitary and Non-tumor

**Begin**

**Initialize**  $P, L$ , and  $R$

**Set** [ $iter = 1$ ]

**While** ( $iter \leq iter_{max}$ )

**For each**  $\eta_\pi$

**Compute** value function

$$v_Q = \sum_R Q(R | P) \sum_{P',L} b(P', L | P, R) [L + \gamma' v_Q(P')]$$

Update  $Q$  value

$$N = \frac{1}{k} \sum \frac{v_Q(P) \times \log(Q(R | P))}{L}$$

End For

End While

Obtain Glioma, Meningioma, Pituitary and Non-tumor

End

Lastly, the CEHJB-RL classifies the types of BT as meningioma, non-tumor, glioma, and pituitary.

## 4 Results and Discussion

Here, the proposed system's performance is authenticated by comparing it with conventional approaches and it is implemented on the platform of PYTHON.

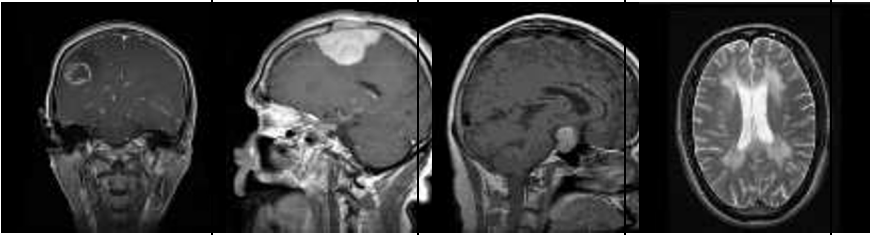
### 4.1 Dataset Description

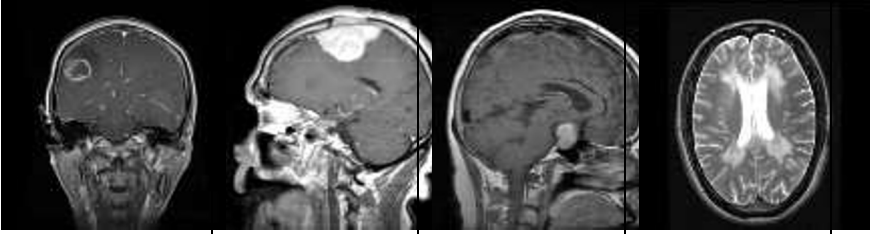
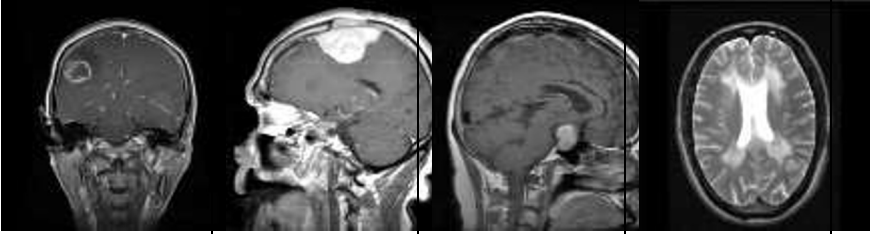
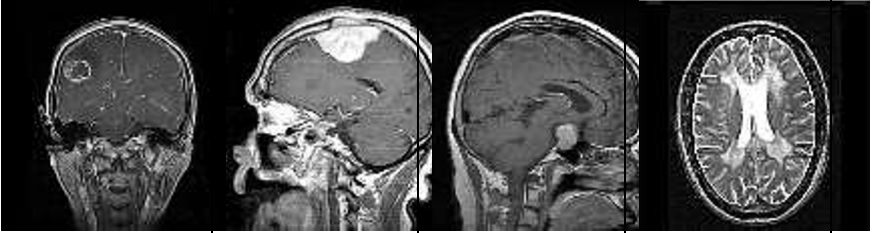
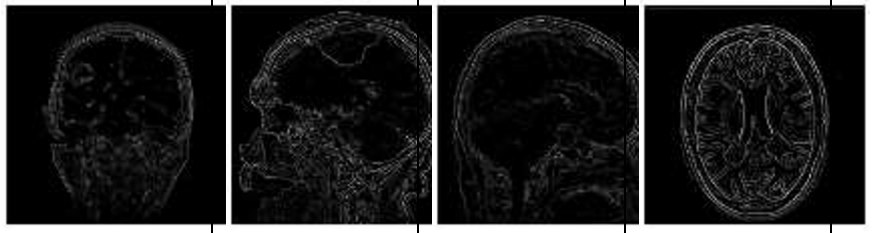
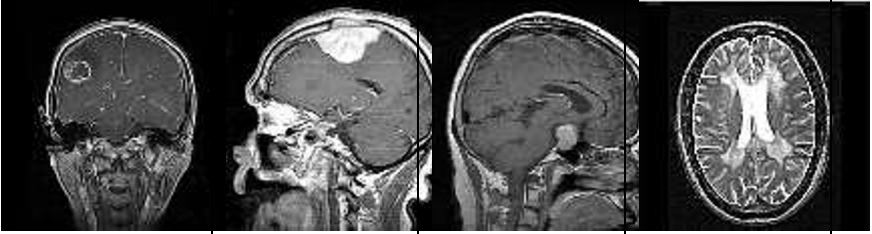
The dataset named BT MRI Dataset (BTMD) [21] is utilized for assessing the proposed framework, which is mentioned in the reference section. The BTMD comprises 7023 brain MRI images, which are categorized as meningioma, non-tumor, glioma, and pituitary. From the whole data, 80% is wielded for training and 20% is utilized for testing, which is explicated in Table 1.

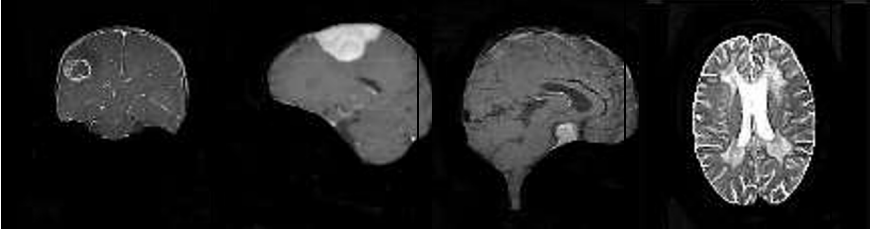
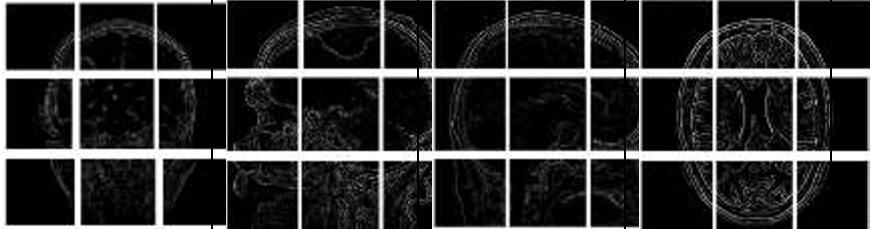
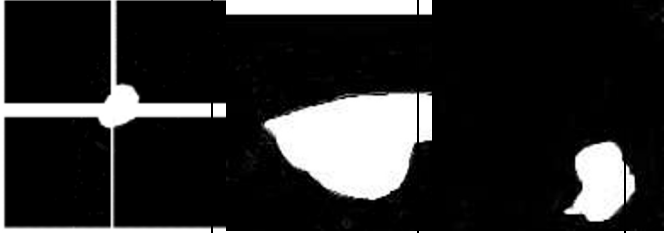

**Table 1.** Dataset characteristics

Tumor Types		Training	Testing
Glioma		1321	300
Meningioma		1339	306
Pituitary		1595	405
No tumor		1457	300
<b>Total samples</b>	7023	5712	1311

**Table 2.** Displays the proposed mechanism's sample image results.

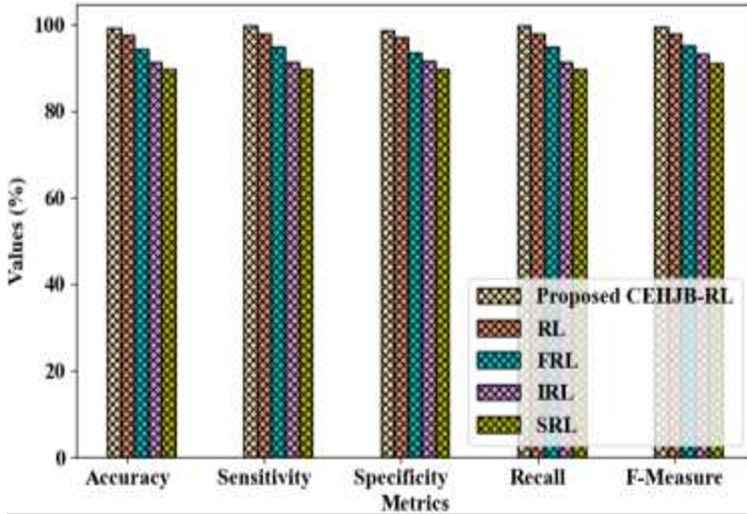
Tumor type	Glioma	Meningioma	Pituitary	No tumor
<b>Input MRI</b>				

<b>Intensity Normalization</b>				
<b>Noise Removal</b>				
<b>Sharpening</b>				
<b>Edge Detection</b>				
<b>With Skull</b>				

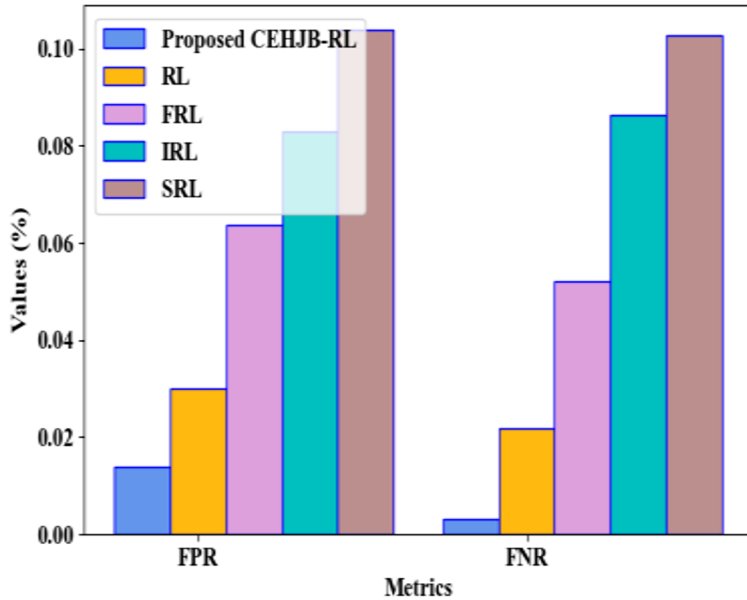
<p><b>Without Skull</b></p>				
<p><b>PE</b></p>				
<p><b>MO</b></p>				
<p><b>Skull between</b></p>				

**4.2 Performance Analysis**

Here, the proposed framework is validated to prove the model's reliability.



(a)



(b)

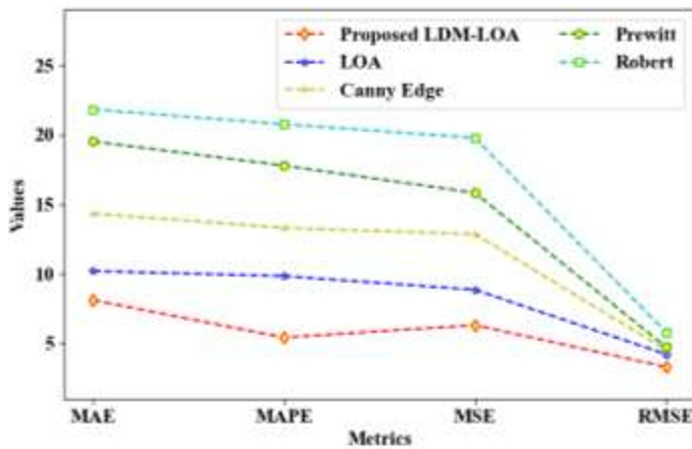
**Fig. 3.** Performance analysis regarding (a) accuracy, sensitivity, specificity, recall, and F-measure, (b) False Positive Rate (FPR) and False Negative Rate (FNR)

The performance validation of the proposed CEHJB-RL and existing methodologies like RL, Fuzzy RL (FRL), Inverse RL (IRL), and Safe RL (SRL) are exemplified in Figure 3. The proposed CEHJB-RL achieved an accuracy of 99.27%, sensitivity of 99.70%, specificity of 98.61%, recall of 99.70%, and F-measure of 99.39%. The FPR and FNR attained by the proposed CEHJB-RL are 0.01% and 0.02%. However, the existing classifiers achieved accuracy, sensitivity, specificity, recall, and F-measure of 93.22%, 93.43%, 92.99%, 93.43%, and 94.37%, respectively. The traditional methods attained the FPR and FNR of 0.07% and 0.06%. The proposed work employs the CEHJB to categorize the BT types, which enhances computational efficiency.

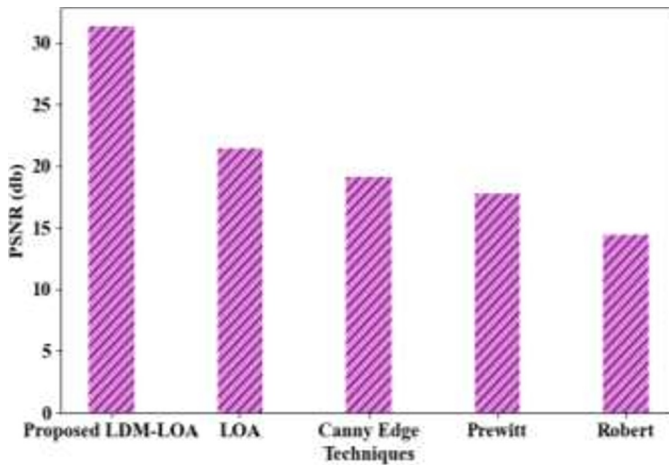
**Table 3.** TT validation

Methods	TT
Proposed CEHJB-RL	57069
RL	65010
FRL	78006
IRL	87015
SRL	97004

Table 3 elucidates the proposed CEHJB-RL’s TT validation. The proposed CEHJB-RL attained a minimum TT of 57069ms, while traditional techniques achieved an approximate TT of 81758ms. The proposed work retained low time complexity.



(a)



(b)

**Fig. 4.** Performance assessment regarding (a) Mean Absolute Error (MAE), Mean Absolute Percentage Error (MAPE), Mean Squared Error (MSE), and Root MSE (RMSE) and (b) Peak Signal-to-Noise-Ratio (PSNR)

Figure 4 displays the proposed LDM-LOA's performance analysis. Here, the proposed LDM-LOA is contrasted with conventional algorithms like LOA, Canny Edge, Prewitt, and Robert. The proposed LDM-LOA acquired MAE of 8.12, MAPE of 5.43, MSE of 6.32, RMSE of 3.32, and PSNR of 31.32db. But, existing methods reached an average MAE, MAPE, MSE, RMSE, and PSNR of 16.46, 15.42, 14.33, 4.83, and 18.20db, respectively. Hence, to improve the optimization results, the proposed LDM-LOA employs the linear density matrix.

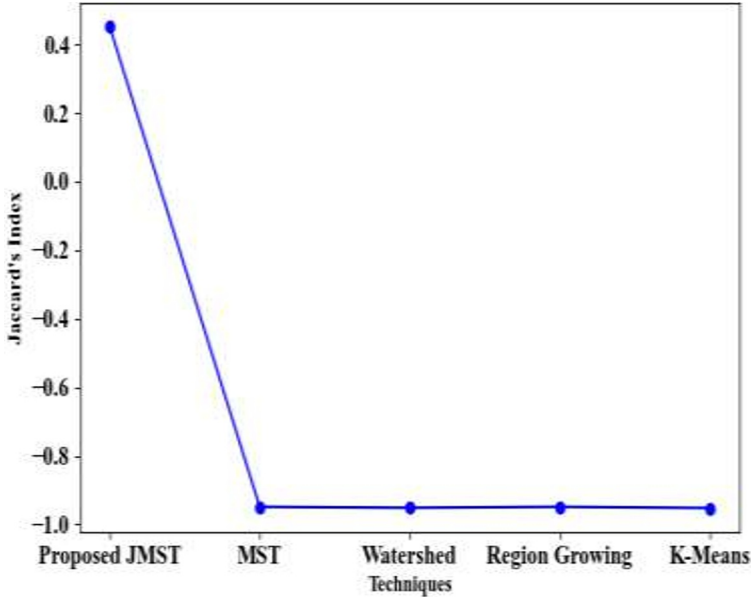


**Fig. 5.** Analysis of JI

The performance of the proposed JMST and traditional methods like JMST, MST, watershed, region growing, and k-means is validated regarding Jaccard's Index (JI) in Figure 5. To enhance the process of graph construction, the proposed JMST incorporates the JS. The proposed JMST achieved a JI of 0.45, while the conventional techniques obtained an average JI of 0.95. The analysis portrayed the high prominence of the proposed model.

**Table 4.** DS assessment

Methods	Dice Score
Proposed JMST	0.82
MST	0.73
Watershed	0.67
Region Growing	0.61
k-means	0.58

Table 4 validates the proposed JMST with existing systems concerning Dice Score (DS). The proposed JMST achieved a high DS of 0.82 owing to its better performance. However, the traditional algorithms retained an approximate DS of 0.65. The research methodology acquired more impressive results than the prevailing works.

## 4.2 Comparative Analysis

To validate the model's efficiency, the proposed model is contrasted with prevailing works.

**Table 5.** Comparative analysis

Works	Algorithms	Accuracy (%)	Precision (%)	Specificity (%)
Proposed model	CEHJB-RL	99.27	99.09	98.61
Amin, Sharif, Yasmin, et al., 2020 [16]	SVM	97.1	-	96.7
Rammurthy & Mahesh, 2022 [17]	WHHO-DCNN	81	-	79
Majib et al., 2021 [18]	VGG-Net	-	99.1	-
Khalil et al., 2020 [19]	DA and level set	98.15	92.55	-
Khairandish et al., 2022 [20]	CNN-SVM	98.49	-	-

In Table 5, the proposed framework's performance is contrasted with existing works. The conventional systems establish techniques like SVM, Whale Harris Hawks Optimization-Deep CNN (WHHO-DCNN), Visual Geometry Group-Network (VGG-Net), Dragonfly Algorithm (DA), and CNN-SVM to achieve BT detection. The proposed CEHJB-RL attained higher accuracy (99.27%), precision (99.09%), and specificity (98.61%). The CEHJB-RL achieved better performance than the conventional techniques.

## 5 Conclusion

This article proposed a dominant approach named CEHJB-RL and JMST-based detection of BTs and types' classification utilizing MRI. The tumor types are proficiently categorized by the proposed CEHJB-RL. By utilizing the BTMD dataset, the proposed system was implemented. The proposed CEHJB-RL attained a better rate of accuracy (99.27%) and recall (99.70%), which proved the model's trustworthiness. The proposed system takes a minimum TT of 57069ms, which displays the low time complexity. Lastly, in tumor types' classification, the proposed work achieved superior performance. Nevertheless, the proposed model focused only on the type's classification of tumor.

**5.1 Future Scope** To enhance the model's superiority, this paper will focus on assessing the severity level of classified tumors in the future.

## Reference

1. D.M. Kumar, D. Satyanarayana, M.N.G. Prasad, *Journal of Ambient Intelligence and Humanized Computing* **12**, 2867 (2021)
2. T. Saba, A.S. Mohamed, M. El-Affendi, J. Amin, M. Sharif, *Cognitive Systems Research* **59**, 221 (2020)
3. P.K. Chahal, S. Pandey, S. Goel, *Multimedia Tools and Applications* **79**, 21771(2020)
4. M.I. Sharif, J.P. Li, J. Amin, A. Sharif, *Complex and Intelligent Systems* **7**, 2023 (2021)
5. M.I. Sharif, J.P. Li, M.A. Khan, M.A. Saleem, *Pattern Recognition Letters* **129**, 181 (2020)

6. J. Amin, M. Sharif, M. Raza, T. Saba, R. Sial, S.A. Shad, *Neural Computing and Applications* **32**, 15965 (2020)
7. Y. Bhanothu, A. Kamalakannan, G. Rajamanickam, *Detection and Classification of Brain Tumor in MRI Images using Deep Convolutional Network*, in proceedings of 6th International Conference on Advanced Computing and Communication Systems, *ICACCS*, 6-7 March 2020, Coimbatore, India (2020)
8. S. Deepak, P.M. Ameer, *Journal of Ambient Intelligence and Humanized Computing* **12**, 8357 (2021)
9. M.A.B. Siddiaue, S. Sakib, M.M.R. Khan, A.K. Tanzeem, M. Chowdhury, N. Yasmin, *Deep convolutional neural networks model-based brain tumor detection in brain MRI images*, in proceedings of the 4th International Conference on IoT in Social, Mobile, Analytics and Cloud, *I-SMAC 2020*, 7-9 October 2020, Palladam, India (2020)
10. P. Windisch, P. Weber, C. Fürweger, F. Ehret, M. Kufeld, D. Zwahlen, A. Muacevic, *Neuroradiology* **62**, 1515 (2020)
11. A. Rehman, M.A. Khan, T. Saba, Z. Mehmood, U. Tariq, N. Ayesha, *Microscopy Research and Technique* **84**, 133 (2021)
12. E. Irmak, *Iranian Journal of Science and Technology - Transactions of Electrical Engineering* **45**, 1015 (2021)
13. R. Mostafiz, M.S. Uddin, N.A. Alam, M.M. Hasan, M.M. Rahman, *Evolutionary Intelligence* **14**, 1075 (2021)
14. Z. Jia, D. Chen, *IEEE Access* **1**, 1 (2020)
15. T. Kalaiselvi, S.T. Padmapriya, P. Sriramakrishnan, K. & somasundaram, *International Journal of Information Technology (Singapore)* **12**, 403 (2020)
16. J. Amin, M. Sharif, M. Yasmin, S.L. Fernandes, *Pattern Recognition Letters* **139**, 118 (2020)
17. D. Rammurthy, P.K. Mahesh, *Journal of King Saud University - Computer and Information Sciences* **34**, 3259 (2022)
18. M.S. Majib, M.D.M. Rahman, T.M.S. Sazzad, N.I. Khan, S.K. Dey, *IEEE Access* **9**, 116942 (2021)
19. H.A. Khalil, S. Darwish, Y.M. Ibrahim, O.F. Hassan, *Symmetry* **12**, 1 (2020)
20. M.O. Khairandish, M. Sharma, V. Jain, J.M. Chatterjee, N.Z. Jhanjhi, *Irbm* **43**, 290 (2022)
21. Dataset, <https://www.kaggle.com/datasets/masoudnickparvar/brain-tumor-mri-dataset>